Laser Shock Peening Induced Back Stress Mitigation in Rolled Stainless Steel

Veronica Over[1]
Department of Mechanical Engineering,
Columbia University,
500 W 120th St.,
New York, NY 10025
e-mail: vho2101@columbia.edu

Y. Lawrence Yao
Department of Mechanical Engineering,
Columbia University,
500 W 120th St.,
New York, NY 10025
e-mail: yly1@columbia.edu

Laser shock peening (LSP) is investigated as a potential tool for reducing tensile back stress, shown here applied to rolled and annealed 304L austenitic steel. The back stress of treated and untreated dog-bone samples is extracted from hysteresis tensile testing. Electron back-scatter diffraction (EBSD) and orientation imaging microscopy (OIM) analysis quantify the geometrically necessary dislocation (GND) density distribution of unstrained and strained as well as unpeened and peened conditions. Finite element analysis (FEA) simulation models back stress and residual stress development through tensile testing and LSP treatment using known LSP pressure models and Ziegler's nonlinear kinematic hardening law. Nonlinear regression fitting of tensile testing stress–strain in as-received specimens extracts the kinematic hardening parameters that are used in numerical study. This research shows LSP may be used to overcome manufacturing design challenges presented by yield asymmetry due to back stress in rolled steel. [DOI: 10.1115/1.4052909]

Keywords: laser shock peening, back stress, kinematic hardening, finite element analysis, recrystallization, laser processes, modeling and simulation

Introduction

Strain history in rolled steel sheets causes there to be a standard tension-compression yield asymmetry along the material's rolling direction (RD) [1]. This yield asymmetry results from residual back stress or a displacement of the material's yield surface due to the Bauschinger effect [2]. Back stress describes the internal frictional stress that resists loading as dislocations pile up at obstacles to glide such as grain boundaries. Residual back stress in as-received material introduces challenges in the design of forming and drawing manufacturing processes and also reduces fatigue life under loading at high-strain amplitudes [3]. In forming and drawing manufacturing, yield asymmetry in as-received material exacerbates the disparity between the levels of hardness and fatigue strength in different areas of a subsequent part [4]. These disparities dictate failure modes and anisotropic behavior corresponding to the shape and method of deformation. Metal spring-back behavior is also of concern during forming, as Bauschinger hardening causes erratic residual plastic strain dependent on the material's loading history [5]. The presence of back stress and kinematic hardening also requires that the design of forming and drawing techniques must be adjusted in order to achieve a desired structure, factoring in an increased number of hardening parameters [6]. As a result, parts such as those used in automotive engines often suffer from misregistry in manufacturing assemblage as strain softening induced by rolling and subsequent metal stamping produces unpredictable final shapes [7]. Further, back stress complicates analyzing fatigue life and requires modified models for failure estimation, standard methods having a tendency to overestimate the life of the part [8,9]. Due to these design challenges, it is of interest to reduce yield asymmetry and general anisotropy in manufacturing rolled-sheet material, especially in materials such as 304L stainless steel whose low corrosive sensitivity and ductility make it attractive for mechanical design.

Annealing heat treatment may eliminate residual anisotropy and strain history in steel, but it also significantly reduces the material's yield strength and alters its design use. Thus, it may be desirable to modify the back stress of a material without reducing its yield. Other methods of reducing yield asymmetry, especially due to strong texture and tortuous grain morphology, are affected through four primary mechanisms: anisotropic strengthening, weakening of texture, and grain-size control. Magnesium alloys and other hexagonal-cubic planed (HCP) metals tend to undergo different modes of plastic deformation in tension and compression, being harder in the direction that is most prone to twinning or according to texture orientations [10–12]. In HCP alloys, unlike FCC metals, precipitates and solid-solution strengthening have uniquely anisotropic hardening modes that can be used to combat characteristic asymmetry [13]. Equal channel angular pressing, multi-directional forging, pre-torsion, and hot extrusion achieve grain refinement and texture weakening through recrystallization [14–17]. These microstructure-control methods tend to be unreasonable for application to rolled steel sheets. The development of a predominant bainite phase reduces the Bauschinger effect in chromolly steel but this is unachievable in austenitic steel [18]. Laser shock peening (LSP) presents a method of back stress reduction that does not significantly alter the grain morphology or phase composition of the material and is therefore attractive for reducing yield asymmetry in stainless steel sheets.

Laser shock peening observably affects microstructure and residual stress in metal targets, making it a potentially promising tool for mitigating tensile back stress along with its more well-known benefits to fatigue and strength performance. LSP is a surface treatment used to improve fatigue life and corrosion resistance of metal parts [19]. LSP directs a high-powered pulsed laser through a transparent confining medium to strike a metal target which is covered in an ablative coating. The ablative layer absorbs the thermal energy of the laser pulse and turns to plasma, rapidly expanding into the ductile surface of the metal due to the constraint of the confining medium. The impact creates shockwaves that emanate through the metal part causing permanent plastic deformation. Several studies report that this process improves texture and refines grain structure, outcomes known to alleviate microstructural anisotropy [19–21]. Compressive residual stress is the most salient feature of LSP that is primarily responsible for arresting crack growth [22]. Similar compressive stress in the surface of gradient nanograined copper induces compressive back stress [23]. It is thus reasonable that investigating applying such a residual stress field to rolled steel may mitigate unwanted tensile back stress by moving the locus of the yield surface in the compressive direction.

[1]Corresponding author.

Manuscript received June 3, 2021; final manuscript received October 26, 2021; published online December 3, 2021. Assoc. Editor: Gary J. Cheng.

This paper shows that LSP indeed reduces the back stress of rolled steel through both microstructural changes and yield surface changes. The back stress of LSPed and as-received samples is compared through hysteresis tensile testing. Electron back-scatter diffraction (EBSD) and orientation imaging microscopy (OIM) analysis examine both control and experimental sample microstructures as well as dislocation distributions before and after strain. Finite element analysis (FEA) of LSP and uniaxial strain employing nonlinear kinematic hardening laws shows peening offsets the yield surface of the material in the compressive direction, measurably reducing the material's bulk back stress.

Background

Kinematic Hardening and Back Stress. Ductile metal kinematically hardens under loading when the central locus of its yield surface offsets in stress space, also known as the Bauschinger effect [24]. The underpinning causes for back stress development have been well discussed in and are widely attributed to the pileup of dislocations at obstacles and grain boundaries [25]. These pileups generate internal friction stress, impeding dislocation glide and increasing the yield stress in the direction of the applied load. After back stress develops in either tension or compression, the material becomes softer when the load is reversed. This softening is due to repelling stresses between dislocations which cause the pileups to rapidly dissipate when loading is reversed, thereby assisting reverse yield. Figure 1 demonstrates the transformation of the yield surface during forward and reverse loading. After initial tensile yield, the material flows in compression at a much lower applied stress due to movement of the yield locus in the tensile direction.

When significant back stress has developed, the displacement of the yield surface due to kinematic hardening may be measured without a full load reversal and can be extracted from tensile loading and unloading hysteresis testing [27]. After undergoing plastic strain followed by unloading, materials with substantial back stress will experience unloading yielding. Unloading yield occurs at the point in unloading when the applied load is equal to the residual back stress due to dislocation pileups. As the applied load further diminishes, the dislocations run back toward their sources away from the obstacles at which they were pinned. The result is a noticeable nonlinearity in the stress–strain curve toward the end of unloading from which it is possible to extract a yield point. It is then assumed that the back stress established before unloading redevelops to the same level through reloading. Extracting reloading and unloading yields from tensile hysteresis enables calculation of the back stress at a given plastic strain. It is then possible to correlate measured back stress with microstructure and dislocation distribution within a material.

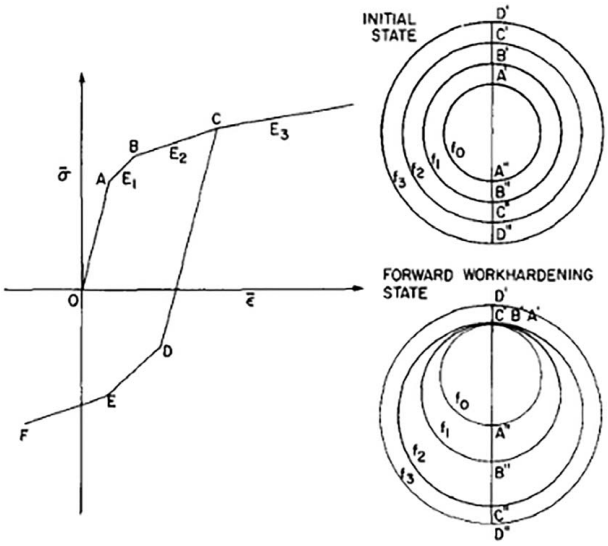

Fig. 1 A loading and reverse loading curve illustrating the Bauschinger effect and the translation and expansion of the yield surface. The initial state shows isotropic expansion of the yield surface and the forward work hardening state depicts the translation of the yield locus under kinematic hardening [26].

Geometrically Necessary Dislocation. Given that kinematic hardening results from dislocation pileups, observation of dislocation distribution gives insight into how back stress develops. Approaches for measuring dislocation density differ according to the type of dislocation. Ashby was first to distinguish between geometrically necessary and statistically stored dislocations (GNDs and SSDs), explaining the residual increase of dislocation density after plastic strain [28]. He established that though dislocation glide is the source of permanent deformation, nonmobile dislocations may be generated under plastic strain either from dislocation sources such as Frank-Reade sources or in order to accommodate strain gradients within grains. The former is the origin of SSDs while the latter is the origin of GNDs. The presence of GNDs within grains results in lattice curvature which can be detected using EBSD and OIM analysis [29,30]. OIM analysis calculates the orientation gradient of each data point taken in an EBSD image. This gradient then correlates directly with GND density, factoring in Burgers vector and the slip systems according to phase. The SSD type is excluded from this analysis because such dislocations do not result from curvature and thus must be observed through direct visual observation such as through transmission electron microscopy. High GND density gradients near grain boundaries in the unloaded state correlate with back stress measurements in large grained tantalum [31]. Dislocations within pileups are spaced increasingly far apart the further from a pinning obstacle they are, resulting in the creation of dislocation gradients. This behavior allows us to extrapolate back stress from the intensity of GND density gradients near barriers to glide. Ex situ measurement complicates this analysis, but even in the unloaded state, a residual dislocation gradient is evident near obstacles such as grain boundaries. SSDs' contribution to back stress has yet to be quantified because they are invisible to OIM. By observing the microstructure and GND density distribution within the LSPed and as-received specimens before and after straining, we can observe the mechanics by which back stress may have been altered between the two groups.

Laser Shock Peening. Laser shock peening increases the fatigue life of metal parts through creating localized plastic deformation in the surface of metal targets. The impact of the expanding plasma generates high-strain rates ($\sim 10^6$ s^{-1}) under the surface of the peened material, creating first elastic then dislocation shock waves emanating from the site of impact [20]. The shock waves dissipate the deeper into the target they penetrate until the waves of applied stress reduces below the material's Hugoniot limit and no further plastic deformation occurs [22]. The plasma expansion forced into the target by the confining medium causes the metal to try to expand outward, but the surrounding material restrains its expansion. This process leaves a profile of compressive residual stress extending typically 0.5–1.2 mm under the surface of the peened part [19]. The compressive force acts to hold closed hairline fractures and cracks, thereby increasing the parts fatigue life. LSP has even been used to heal fissures after they have formed [32]. Compressive residual stress has the effect of resisting tensile applied stress and also assisting reverse yielding. The result is to displace the yield surface of the material in the compressive direction, thereby diminishing tensile back stress. This effect is aided by alterations made to the material's microstructure.

The shock waves produced by LSP create several dislocation fronts which transform from dislocation cells into nano-grains, new grain boundaries and residual dislocations as the shock wave

expands. The resulting grain refinement, dislocation structure, and plastic lattice rotation have been widely observed through transmission electron microscope and EBSD [33–36]. Application of a high enough LSP pressure to 304 stainless steel causes recrystallization, achieving grain refinement producing more equiaxed grains [33]. Below this pressure threshold, the stored strain energy within residual dislocations is such that upon annealing, significant grain refinement and recrystallization can be produced, a tool that has been used to tailor the microstructure of additively manufactured parts [37]. Residual dislocations are also associated with a measured hardness increase local to the LSPed surface [36]. It may be counter intuitive that a process known to create hardening dislocations reduces the back stress of a material given that increased GND density gradient corresponds to increased back stress. However, as detailed by Ashby [28], dislocations in a polycrystalline material have many sources and only generate back stress when they contribute to resisting the applied load. The dislocations created by LSP harden in compression, which is the mode of yield tested by standard hardness tests. However, by kinematically hardening, the material in compression these dislocations assist yield in the material in tension by developing compressive back stress. This effect combined with the compressive residual stress profile, recrystallization, and dislocation annihilation produced by LSP is here shown to contribute to creating a bulk back stress reduction in material with prestrain tensile back stress.

Experimental Procedure. The samples come from 3.175 mm-thick rolled and annealed 304L stainless steel manufactured to the AMS 5511 standard. Wire electrical discharge machining (EDM) cut both control and experimental tensile specimens to a standardized ASTM E8 geometry. Four dog bones were prepared for LSP treatment while four were left as-received; all were cut such that the rolling direction is the same direction as the applied tensile load. A Quanta-Ray Lab Series, Q-switched Nd:YAG Spectra Physics laser was applied LSP to the front and back surfaces of the experimental samples' gauge length. Directed through an acrylic confining medium and set at a 100 Hz rep rate, 10 ns pulse width, and 150 mJ pulse energy the laser ablated a layer of Polyester 3M tape on the surface of the tensile sample below. The two groups of resulting samples are shown representatively in Fig. 2. The diameter of the spot size applied to the surface of the sample is around 400 μm. The stage holding the sample moved at a 40 mm/s and each peen center is located 400 μm from the next in the same row. The resulting plastically deformed peen indentations are smaller than the laser spot size as visualized in Fig. 3 through optical profilometry. An MTS 7k electromechanical machine strained each sample to 3% before unloading to zero load and reloading to 4% total strain (Fig. 4). For EBSD observation, both strained and unstrained samples were cut using wire EDM to maintain the existing stress distribution. Electropolishing with phosphoric acid, sulfuric acid, and glycerin solution at 0.167 A/mm^2 for 10 min prepared samples for microscopy, using Teflon tape to mask the sides. The polishing removed approximately 100 μm of material. Lin and Hu [38] provide the solution chemistry for polishing. EBSD was performed using a Zeiss Sigma VP scanning electron microscope an EDAX Hikari Plus EBSD camera and EDAX TEAM analysis software.

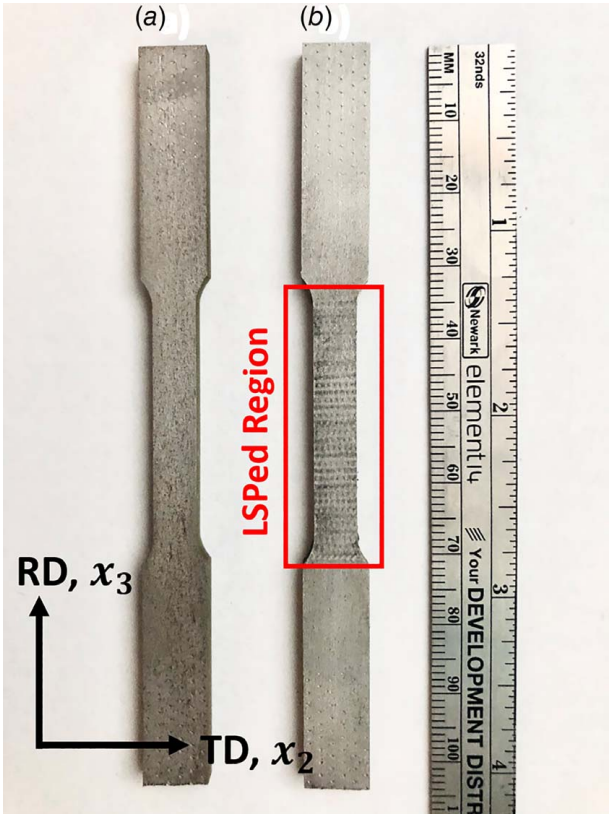

Fig. 2 (*a*) As-received sample and (*b*) LSPed sample. The gauge length has LSP applied to both front and back. The laser ran across the transverse direction at a 40 mm/s speed. Each row is spaced approximately 400 μm apart. The x_2 and x_3 directions identify the axes of the simulation.

Numerical Modeling

Laser shock peening pressure loading and continuum kinematic hardening as modeled by Abaqus simulates experimental results. LSP impacts are applied to the surface of a quarter model of the experimental specimen's gauge length with dimensions 3 mm × 1.5 mm × 3 mm. Twenty pulses are applied to the x_2-axis surface (Fig. 2): five per row and four per column as produced by the 40 mm/s stage speed in the experiment. After peening, a ramped surface load gradually applies 422 MPa in the x_{33} direction to simulate uniaxial tension. Boundary conditions enforce symmetry on three sides for both LSP and uniaxial tensile loading.

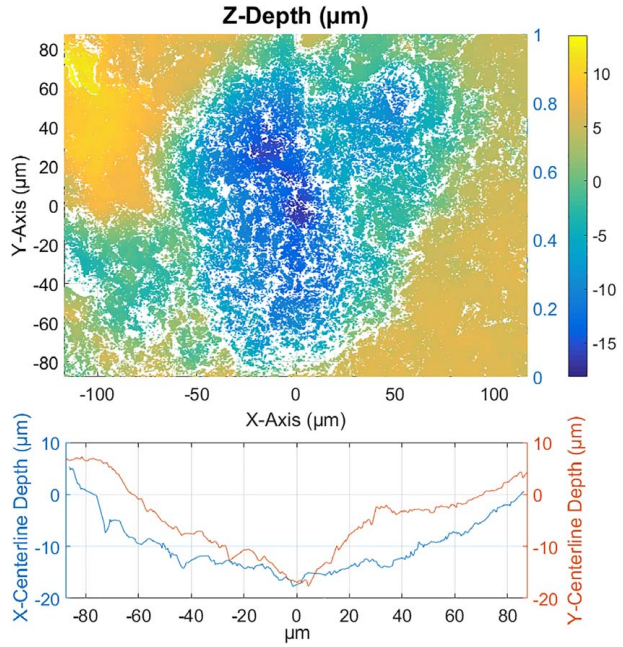

Fig. 3 Representative depth profile of an LSP indent as measured by optical profilometry. The diameter of the observable plastic deformation is approximately 180 μm in both *x* and *y* directions and reaches a depth of 17 μm.

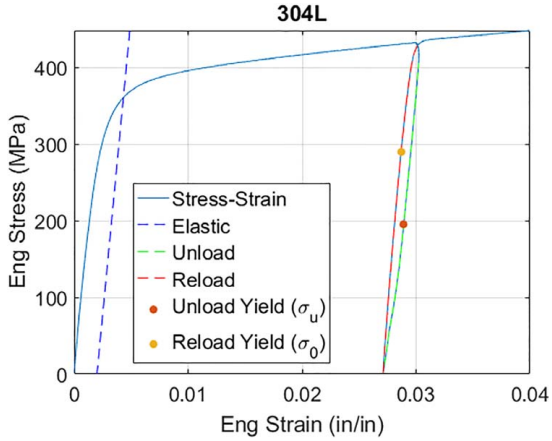

Fig. 4 Typical tensile stress–strain curve in as-received specimens. LSPed specimens showed comparable behavior. The initial plastic yield occurs at the intersection of the dashed elastic line marking a 2% offset from zero elastic strain. The average of the unloading yield and reloading yield is near the measured back stress given that the thermal stress is small.

It is standard to assume that LSP has minimal thermal effect on the surface of the metal target, given that the ablative layer absorbs the majority of the laser's thermal energy and converts it into an expanding plasma [39]. The estimation used here assumes the pressure profile to be Gaussian and the laser pulse intensity develops as a triangle wave with a 10 ns pulse width. Solving the coupled differential equations below calculates peak pressure development:

$$P(t) = \frac{Z}{2}\frac{dL}{dt} \tag{1}$$

$$I_{peak}(t) = \frac{Z}{2}\left(1+\frac{3}{2\alpha}\right)\left(\frac{dL}{dt}\right)^2 + \frac{3}{4}\frac{Z}{\alpha}\left(\frac{d^2L}{dt^2}\right)L \tag{2}$$

where $P(t)$ = peak pressure at the LSP interface as a function of time t, $Z = 2Z_1Z_2/Z_1 + Z_2$ = combined impedance of the LSP interface ($Z_1 = 3960$ kg/cm^2 impedance of steel, $Z_2 = 320$ kg/cm^2 impedance of acrylic), $L(t)$ = peak plasma thickness, α = parametric fraction of internal energy that increases the thermal energy of the plasma, and $I_{peak}(t)$ = peak laser intensity [39,40]. Given the laser intensity, the maximum peak pressure is found to be 6 GPa and $P(t)$ develops approximately according to a triangle wave. A user subroutine supplies the pressure input into the simulation, developing peak pressure as a triangle wave with the same pulse width as the laser.

A standard Hooke's law describes elastic behavior with a Young's modulus of $E = 155.44$ GPa as derived from regression fitting to experimental stress–strain. After von Mises yield, the material undergoes combined kinematic and isotropic hardening. A nonlinear iteration of Ziegler's linear kinematic hardening law models the back stress development after LSP and due to uniaxial tension:

$$\dot{\boldsymbol{\alpha}}_k = \frac{C}{\sigma^0}(\boldsymbol{\sigma}-\boldsymbol{\alpha})\dot{\bar{\epsilon}}^{pl} - \gamma_k\boldsymbol{\alpha}_k\dot{\bar{\epsilon}}^{pl} \tag{3}$$

where $\boldsymbol{\sigma}$ = the stress tensor, $\boldsymbol{\alpha}$ = the back stress tensor, $\boldsymbol{\alpha}_k$ = the kth back stress tensor component, C = kinematic hardening modulus, $\dot{\bar{\epsilon}}^{pl} = \sqrt{2/3\dot{\epsilon}^{pl}:\dot{\epsilon}^{pl}}$ = the equivalent plastic strain rate (ϵ^{pl} = plastic strain), γ = an exponential hardening parameter, and $\sigma^0 = \sqrt{3/2(\boldsymbol{S}-\boldsymbol{\alpha}^{dev}):(\boldsymbol{S}-\boldsymbol{\alpha}^{dev})}$ = the size of the yield surface ($\boldsymbol{S}$ = deviatoric stress tensor, $\boldsymbol{\alpha}^{dev}$ = deviatoric component of the back stress tensor) [41]. Assuming only one additive back stress tensor component and uniaxial tension along the x_{33}, $(\boldsymbol{\sigma}-\boldsymbol{\alpha})$ reduces to $(\boldsymbol{\sigma}-\boldsymbol{\alpha})_{33} = \sigma^0$. Thus, the back stress along the loading direction changes as

$$\dot{\alpha} = (C - \gamma\alpha)\dot{\bar{\epsilon}}^{pl} \tag{4}$$

Integration over half of a loading cycle with an initial pre-strain and back stress yields the following:

$$\alpha = \frac{C}{\gamma}(1 - e^{-\gamma(\bar{\epsilon}^{pl}-\bar{\epsilon}_0^{pl})}) + \alpha_0 e^{-\gamma(\bar{\epsilon}^{pl}-\bar{\epsilon}_0^{pl})} \tag{5}$$

given α_0 = the initial back stress and $\bar{\epsilon}_0^{pl}$ = the initial equivalent plastic strain. With combined isotropic and kinematic hardening, the yield surface size increases exponentially so that the applied stress is given by

$$\sigma = \sigma|_0 + Q_\infty(1 - e^{-b\bar{\epsilon}_0^{pl}}) + \alpha \tag{6}$$

where $\sigma|_0$ = yield stress without strain, Q_∞ = maximum size of the yield surface, and b = the exponential rate of increase of the yield surface size up to the maximum. To model the as-received material, the hardening equation parameters are fit in STATA to measured back stress and experimental stress–strain curves with. Further parameter exploration finds the closest match with the LSPed experimental data. First, the back stress hardening Eq. (5) is fit to the measured back stress and strain, yielding $\alpha_0 = 150$ MPa, $\bar{\epsilon}_0^{pl} = 0.022$, $\gamma = 50$, and $C = 1.19$ GPa ($R^2 = 0.97$). The back stress hardening equation with fit parameters is then input into isotropic hardening Eq. (6) whose parameters are fit using stress–strain data. The resulting fit parameters are $\sigma|_0 = 256$ MPa, $b = 300$, and $Q_\infty = -0.593$ MPa ($R^2 = 0.77$). This initial yield and initial equivalent plastic yield indicate that the material is indeed prestrained. The Q_∞ value indicates a moderate contraction of the yield surface. Contraction has been observed to be a feature of a flattening of the yield surface due to kinematic hardening [42]. To model LSP, high-strain rate material properties are also required as an input into the model. The high-strain rate yield ratio up to 10^4 is taken from the literature [43]. Both the LSP and tensile loading were implemented in ABAQUS Explicit.

Results and Discussion

Back Stress Determination. Tensile testing conducted on as-received and LSPed specimens allowed comparison of stress–strain and back stress development. Each specimen was strained to 3% before unloading to zero load and reloading to 4% total strain. The testing was repeated on four specimens of each group. A typical stress–strain curve may be seen in Fig. 4 for an as-received specimen and LSPed specimens show similar patterns. The average 2%-offset initial plastic yield is measured as 343.3 MPa and 360.9 MPa for as-received and LSPed groups, respectively. The LSPed samples demonstrate a compressive yield surface offset upon both tensile and hysteresis loading. Softening of the tensile yield in the shock treated group supports findings from unloading–reloading analysis showing back stress was reduced in the LSPed samples as compared with the control specimens.

To derive back stress from stress–strain hysteresis, plastic and elastic responses must be individuated. Unloading and reloading yield are used in calculating back stress:

$$\sigma_b = \frac{\sigma_u + \sigma_0}{2} - \frac{\sigma^*}{2} \tag{7}$$

where σ_u = unloading yield stress, σ_0 = reloading yield stress, and σ^* = thermal relaxation component of plastic flow [27]. The thermal flow adjustment (σ^*) factors in creep relaxation at the start of unloading. In the original formulation of deriving back stress from unloading–reloading hysteresis, Yang et al identifies unloading yield as a 5%–15% deviation from elastic behavior [27]. As seen in Fig. 5, the unloading stress–strain has a distinct elastic regime as demonstrated by the flattened portion of the

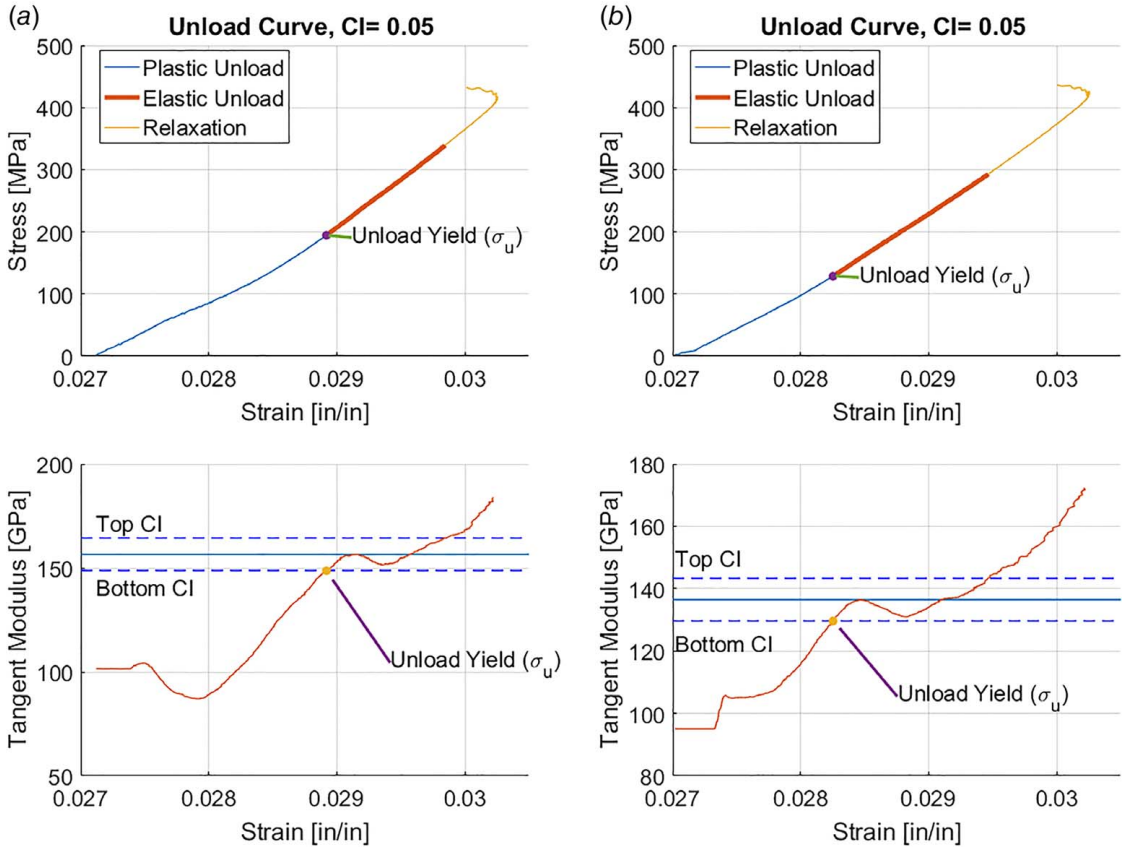

Fig. 5 Unloading curve and unloading yield definition at 3% strain for (*a*) an as-received sample and (*b*) an LSPed sample. The elastic response is defined as occurring between the top and bottom CI which is ±5% of the elastic unloading modulus. The LSPed sample exhibits a longer elastic response with a lower unloading yield, therefore indicating a lower back stress.

tangent modulus. The tangent modulus is evaluated by calculating the regression slope of a neighborhood of 65 points at each point of the unloading curve. This number of points allows a sufficient amount of smoothing to reduce noise. The slope of the tangent modulus curve is then calculated using 20 neighboring points and the minimum point of the second-derivative of the unloading curve is considered the center of the elastic response. The tangent modulus at the center of elastic unloading is the adjusted elastic modulus or the unloading elastic modulus (E_u). The unloading yield (σ_u) is marked as the lowest stress during unloading that has a 5–15% deviation from E_u. The highest stress of the reloading curve that has a 5–15% deviation from the E_u marks the reloading yield point (σ_r). Thermal relaxation stress (σ^*) is calculated as the difference between the stress at the beginning of unloading and the stress at the beginning of the unloading elastic regime.

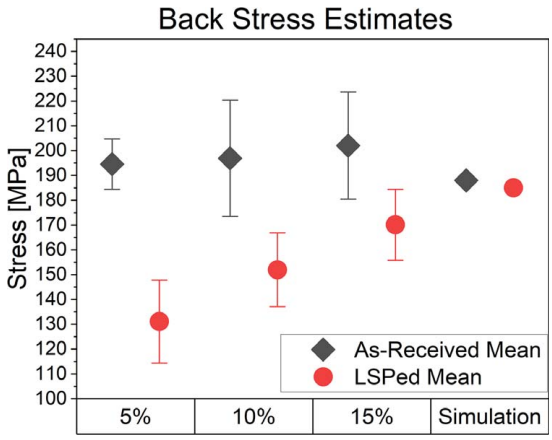

Fig. 6 Back stress in the as-received and LSPed samples at all unloading yield definitions and from simulation. The bars represent standard deviation. Back stress results are calculated with the unloading yield evaluated at 5%, 10%, and 15% deviation from elastic behavior, demonstrating a reduction in LSPed samples for all three definitions. The simulation results after pulling show only a 3.5 MPa reduction in bulk-averaged back stress as compared with the as-received sample, which is discussed below.

The average back stress of the LSPed materials at 5%, 10%, and 15% unloading yield definitions are 131.1 MPa, 152.0 MPa, and 170.1 MPa, respectively. The back stress of the as-received samples at 5%, 10%, and 15% unloading yield definitions are 194.5 MPa, 196.9 MPa, and 202.0 MPa, respectively. Figure 6 shows the distribution of back stress calculations according to each definition and compares the result with simulation. The difference between the LSPed and as-received samples is most prominent at the 5% yield definition. As seen in Fig. 5, the as-received material has an elastic regime that ends at a higher stress and that is also shorter than in the LSPed material, indicating a higher back stress. On average, the back stress reduction under these three definitions is 23.7%, which is not insignificant and indicative of the effectiveness of LSP in reducing back stress under the conditions investigated.

Numerical Simulation. Although the simulation also shows a back stress reduction by LSP, the model underestimates the bulk-averaged reduction to back stress after strain, compared with experimental results in Fig. 6. However, this is likely because it does not factor in microstructural changes such as recrystallization.

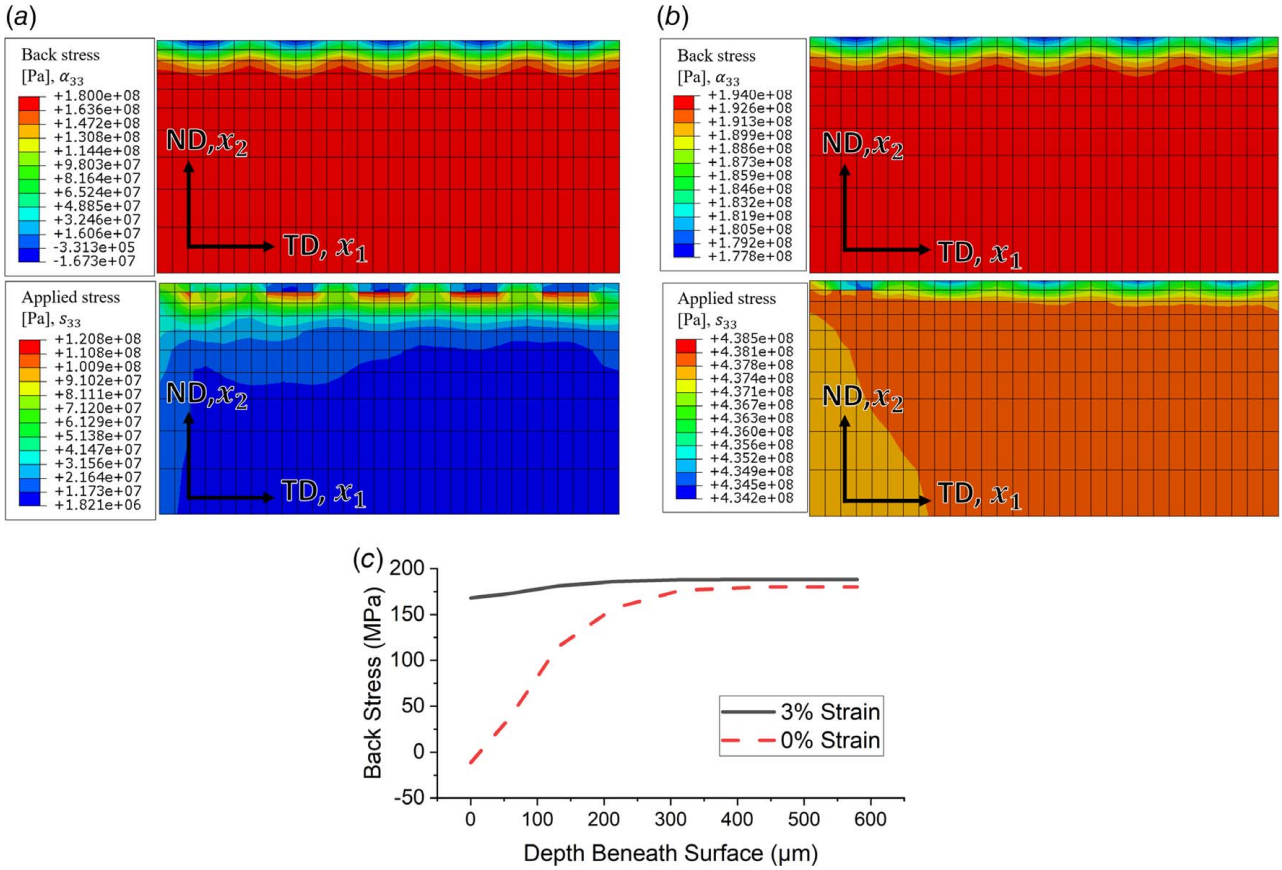

Fig. 7 Cross section of simulation results in an LSPed sample showing uniaxial applied stress (s_{33}) and back stress (α_{33}) (*a*) before tension and (*b*) after 3% strain. As seen in (c) the back stress is reduced by LSP in a layer up to 250 μm deep directly under the cite of peening. This reduction near the LSPed surface is lessened after pulling but the depth of the affected area remains the same. The residual stress reduction penetrates to 350 μm, but the depth of the residual stress diminishes after strain.

Furthermore, the material response modeled by implicit Abaqus rate-dependent plasticity is a simplification of the true hydrodynamic fluid-like behavior of the material at high strain [44]. Simulation also assumes only a single component of the back stress tensor to refrain from over fitting the data; a larger data set fit with multiple back stress components may create a more accurate reduction. Simulation shows that with increased pressure and or with multiple LSP applications the reduction improves. It is feasible that with increased LSP density and increased laser power, back stress could be reduced further. The modest reduction to the bulk back stress within the simulation model shows that microstructural changes that are not accounted for in the numerical simulation play a dominant role in adjusting the sample's yield surface.

To further explore the simulation results, spatially resolved back stress distributions are investigated. Simulation identifies that LSP treatment locally reduces the pre-existing back stress near the surface, an effect that lasts through uniaxial tension. Figure 7 demonstrates that the maximum reduction to the back stress occurs at the surface at the point on the material that experiences the highest pressure due to LSP. The decrease is extremely local to the region of plastic strain region due to LSP and decays exponentially outward from the point of impact up to a depth of 250 μm. At the point of peak applied pressure, the reduction changes the back stress 180 MPa to −16.7 MPa. The back stress profile after LSP is unlike the residual stress profile which shows the maximum reduction after peening occurs at a depth of 130 μm with a compressive residual stress of −94.5 MPa but the depth of compressive stress extends to 350 μm. Evidently the compressive plastic flow nearest the point of peening relaxes the residual stress while maximally reducing the back stress. After strain, the back stress increases according to Eq. (3), and the difference between the surface and center of the material reduces. If uniaxial tension were to continue, the difference would eventually diminish entirely. The residual stress reduction decays by an even greater extent after strain and the depth of affect is also reduced.

Electron Back-Scatter Diffraction Analysis. EBSD imaging and TSL OIM analysis of the microstructures of control and experimental samples construes the yield surface displacement made due to grain morphology and dislocation distribution changes. The majority of the microstructure in both LSPed and as-received samples is austenite. EBSD phase identification reveals the as-received composition was 90.5% austenite, 8.7% cementite, 0.2% martensite, 0.5% iron epsilon, and 0.1% iron alpha. The LSP composition was nearly the same showing 90.5% austenite, 8.6% cementite, 0.1% martensite, 0.6% iron epsilon, and 0.1% iron alpha. Multiple images were taken of the top surface (RD × transverse direction (TD)) as well as of the cross section (normal direction (ND) × (TD)) though only a representative four images are presented here with different analysis processing.

Inverse Pole Figure and Texture. Inverse pole figure (IPF) images (Fig. 8(*a*)) of the as-received unstrained material show weak texture and identifiable orientation gradients within large grains especially near grain boundaries. Residual effects of rolling manufacturing are observable. Several grains are slightly elongated along the RD and also contain mechanical twins primarily sheared along the RD. Clusters of small grains and annealing twins likely resulted from recrystallization due to heat treatment but it is

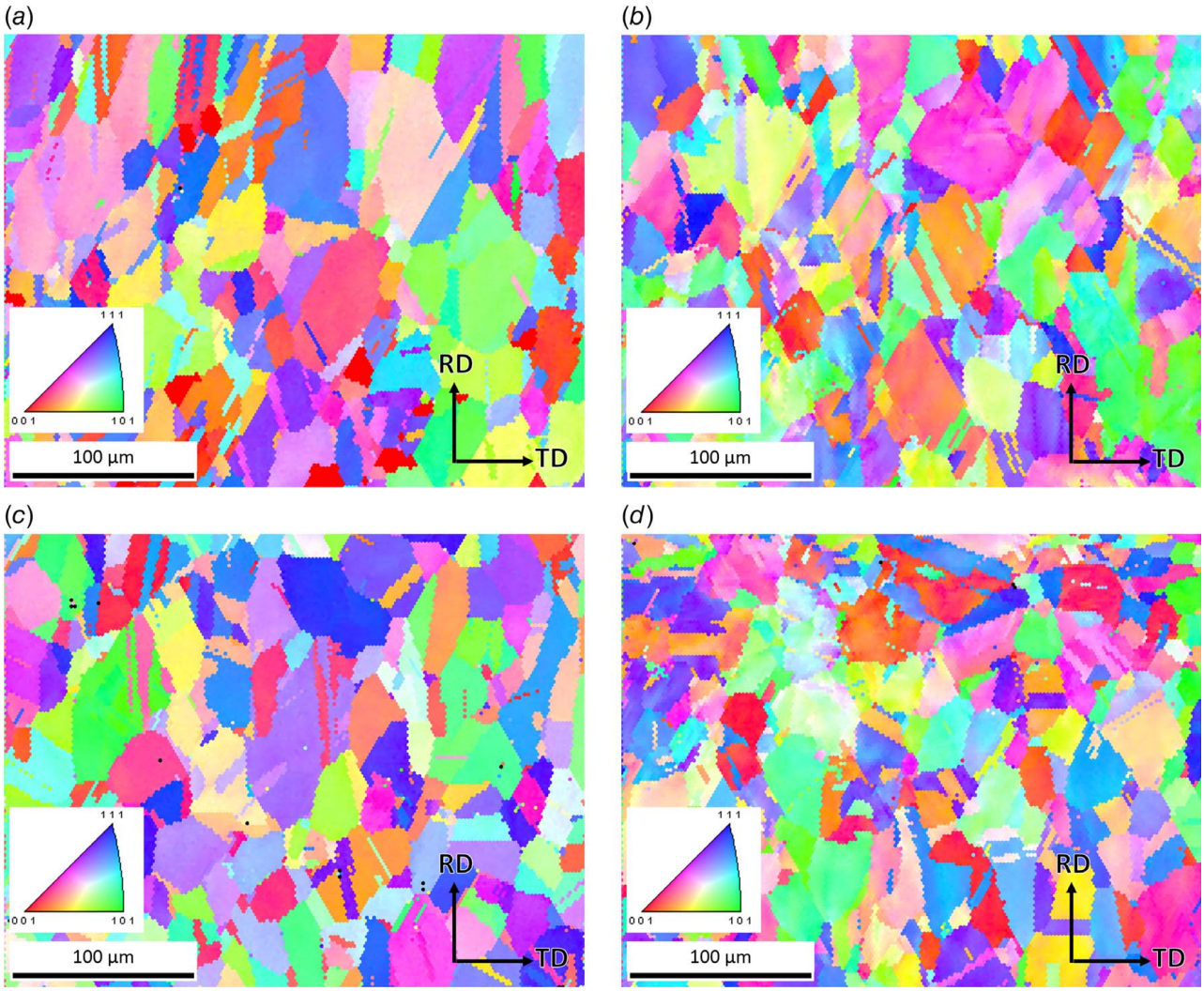

Fig. 8 IPFs of top surface in the as-received samples in (*a*) unstrained and (*b*) 4% strained conditions and LSPed samples in (c) unstrained and (*d*) 4% strained conditions. Moderate grain refinement and an increase of equiaxed grains can be observed in the LSPed samples both before and after plastic strain.

evident that the temperature increase was not held long enough to sustain complete stress relief and grain renewal. The average grain size is 10.82 μm in diameter. After LSP (Fig. 8(*c*)), the microstructure has fewer long thin grains with an increase in the fraction of equiaxed grains free of twins or else with lenticular recrystallization twins. This has been previously noted to evidence the creation of new grains due to dislocation shock wave expansion [33]. There is still some residual mechanical twinning along the RD in large grains. After straining to 4% total strain, both the as-received samples and LSPed samples (Figs. 8(*b*) and 8(*d*)) have much more pronounced orientation gradients within both large and small grains, as well as significantly more twinning and a larger representation of small grains which is typical of plastic strain.

Geometrically Necessary Dislocation Distribution. The lack of a strong texture and very large grains in the as-received sample along with the evident high unloading yield measured in tensile testing indicates dislocation pileups are dominant in contributing to yield asymmetry in rolled and annealed 304L steel. TSL OIM analysis directly observes GND distribution, using the austenite FCC $\{111\}[1\bar{1}1]$ slip system for calculation. As seen in Fig. 9(*a*), the as-received material shows a level of GND density of pileups near grain boundaries and near twins, as a result of rolling. Within around 50 μm of the LSPed surface, there is observed a moderate increase in level of GND density as compared with the as-received samples (Fig. 10(*c*)). However, at 100 μm deep, the LSPed sample exhibits a slightly lower intensity of such dislocation pileups with a distinctly lower peak density near grain boundaries (Fig. 10(*c*)). After straining, both LSPed and as-received samples show significant increase in GND density in general, GND pileups occurring along planes that are close to twinning shear and near the end of lenticular twins in particular. It is important to note such GND dislocation pileups are more severe in as-received sample than the LSPed sample under strained condition. Thus, LSP reduces back stress. Pileups are also most intense within small grains showing maximum GND density near grain boundaries.

Plotting the GND density against their distance to the nearest grain boundary quantifies the GND density gradient near obstacles to glide which illuminates the mechanism by which LSP reduces back stress. To reduce noise, data points with higher than a 100 $10^{12}/m^2$ GND density were omitted from this qualification. In this calculation, the grain boundary is defined as a scan point that contains a boundary with at least a 15 deg misorientation relative to its neighbor. Each EBSD point has a set of coordinates in μm within the EBSD scan. Dependent on the EBSD step size, the scan records data at either 1 μm, 1.5 μm, or 2 μm increments in x and y. The distance between a given data point and all grain boundary points is calculated and the minimum of these distances is taken

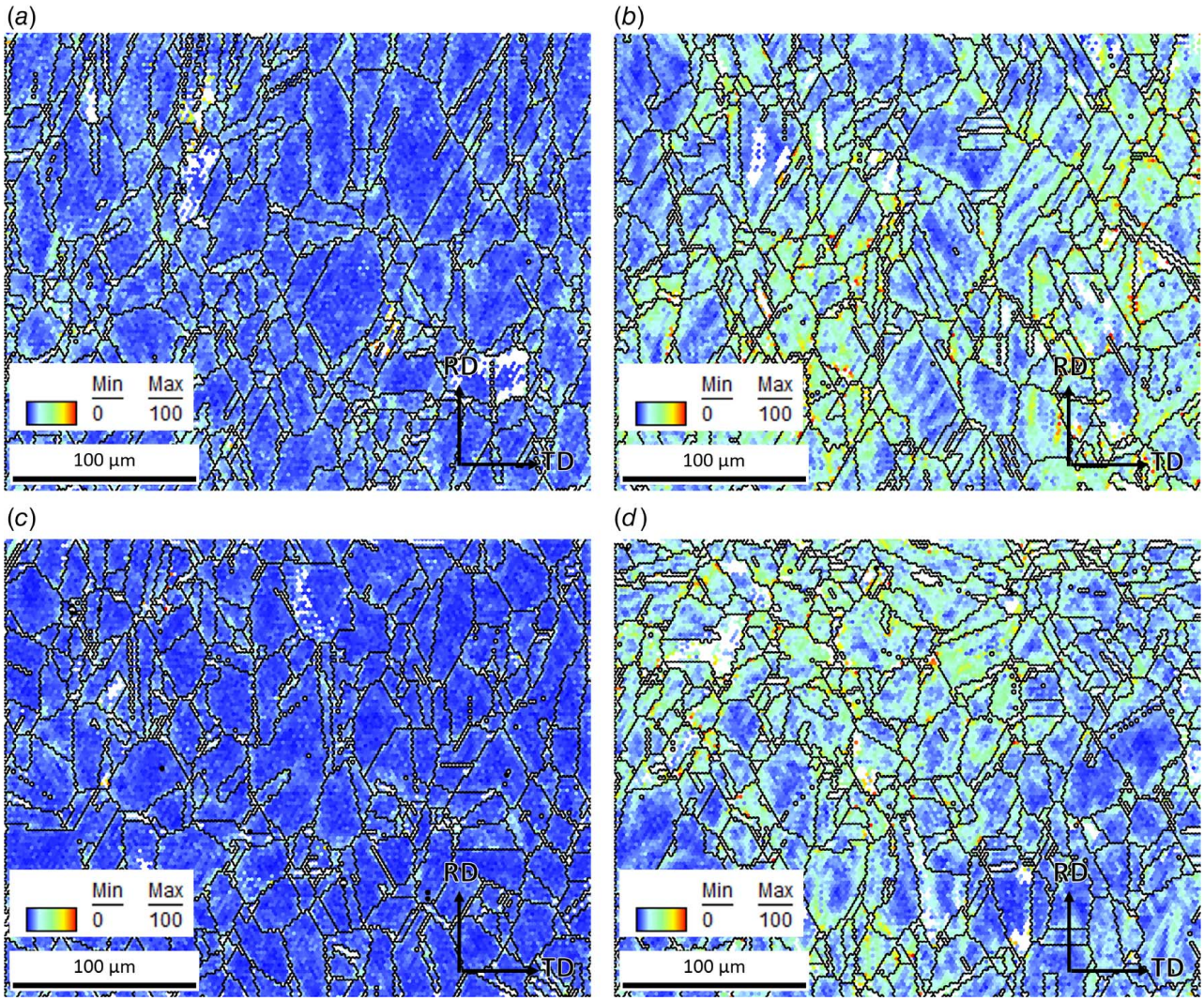

Fig. 9 GND density maps of the top surface in the as-received samples in (*a*) unstrained and (*b*) 4% strained conditions and LSPed samples in (c) unstrained and (*d*) 4% strained conditions. The color bar range is between 0 and 100 $10^{12}/m^2$. Blank areas are above this range and are excluded to reduce overestimation noise as recommended in the TSL OIM manual. The grain boundaries are defined as 15 deg misorientation. The as-received and strained material (Fig. 9(*b*)) exhibits higher GND density accumulation near grain boundaries than in the LSPed and strained material (Fig. 9(*d*)).

as the distance of that point to the nearest grain boundary. Due to the discrete step size of the EBSD scans, the nearest distance calculation is discrete, with the minimum distance being 0 μm the next distance being 1 μm. Thus, average GND density is calculated by binning each scan point into a rounded-down distance bin and taking the average of each bin.

From the plots in Fig. 10(*a*), it is evident that at depth of 100 μm the level of GNDs is slightly reduced after LSP and this result is sustained through uniaxial tension, especially as seen in the top surface. Before straining, the GND density and gradient is slightly higher in the as-received sample. The gradient difference is small but still distinct. A regression analysis finds that the slope of the as-received GND-distance data is −0.77, while the slope of the LSPed GND-distance data is −0.68. After straining, the GND density level increases in both the as-received and LSPed samples. The level of GNDs in as-received samples after strain is higher than in the LSPed and strained samples. However, the GND density gradient is increased in the LSPed sample after strain with a slope of −1.18 compared with the −0.87 slope in the as-received sample. Noted also is that the magnitudes of both of these slopes are increased along with the level of GND density as compared with the unstrained samples.

Evaluating dislocation pileups ex situ is a challenge because upon unloading, dislocations run back to their sources, thus homogenizing the distribution of GND density and softening in reverse loading. In a loaded state, a high GND density gradient near grain boundaries is indicative of dislocation pileups which contribute to back stress and assist reverse loading when they flow away from their pinning barriers. However, in an unloaded state, an increased level of homogenous GNDs may still indicate high back stress because once loading begins, these evenly distributed dislocations are likely to run back toward pinning barriers, redeveloping dislocation gradients and arresting dislocation glide. From this understanding coupled with the parameters discovered in the nonlinear fit of the continuum back stress laws, it is possible to construct a narrative. In the as-received material, back stress was predeveloped to 150 MPa (according to the nonlinear fit of Eq. (5)) with pre-existing GND pileups. LSP reduced the dislocation pileups and thus back stress. Tension and subsequent unloading caused the as-received sample to experience more reverse plastic strain than the LSPed sample going through the same loading–unloading regime. This is due to the higher back stress initially present in the as-received material which increased the unloading yield so that reverse yielding occurs for longer than in the LSPed sample. This longer regime

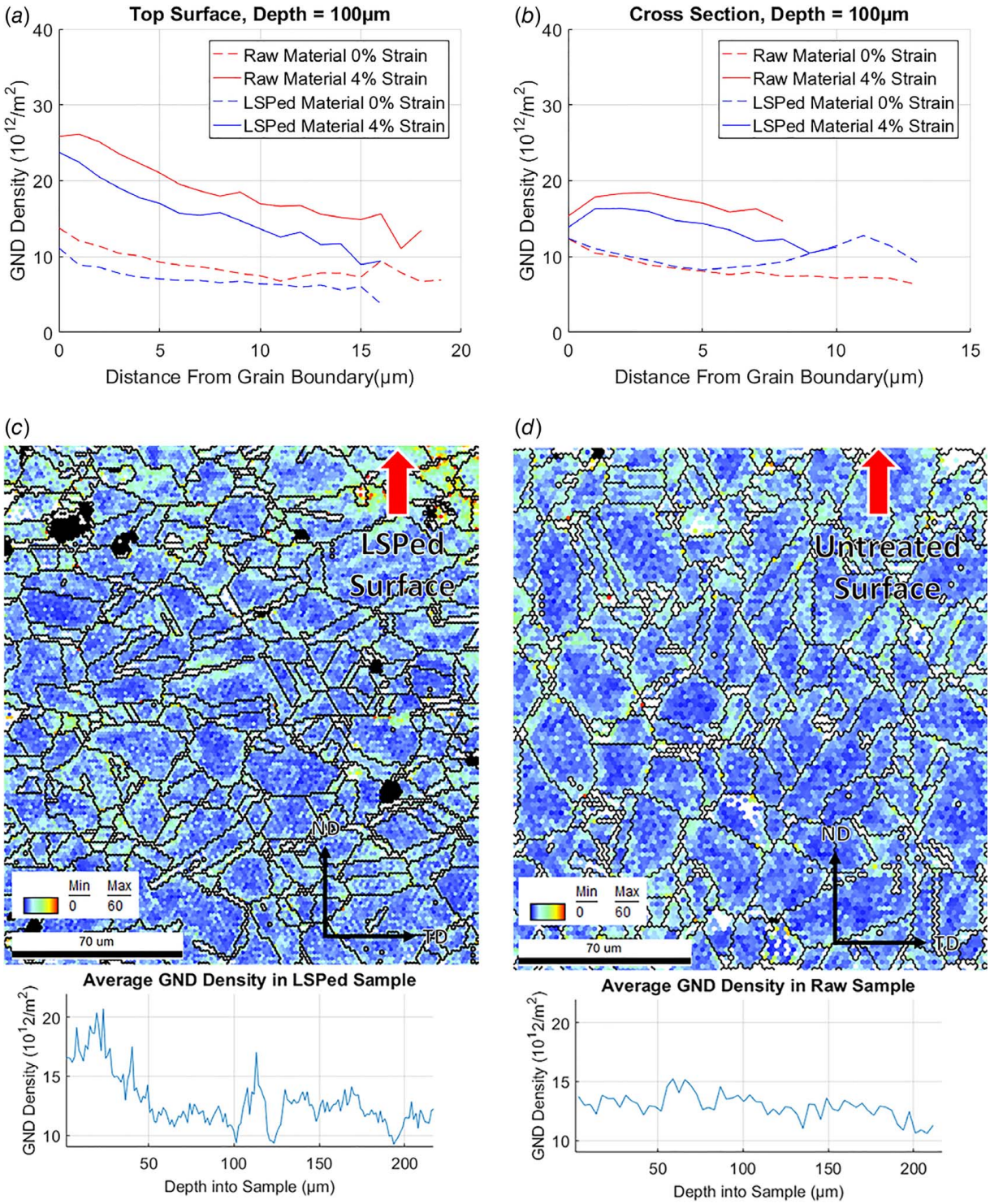

Fig. 10 Average GND density versus distance from grain boundary in the top surface (*a*) and in the cross section (*b*) at 0% and 4% strain provided for both LSPed and as-received materials. Cross-sectional images taken before tensile strain (*c* and *d*) show a marginal increase of GNDs near the peened surface as compared with the untreated sample. The cross-sectional measurements in (*b*) are taken at 100 μm beneath the top surface. The top surface images are taken at 100 μm deep due to the depth of polishing show a higher GND density level in the as-received material in both strained and unstrained materials. The GND density gradient is higher in the as-received material before strain but not after. The cross section shows no GND density gradient in either sample.

of reverse yield decreases the number of GND pileups at the grain boundaries while still maintaining a higher level of GND density overall. In cross-sectional images, neither the raw nor the LSPed samples exhibit significantly high GND density gradient. This is a logical result because the TD and ND directions do not have known yield asymmetry or back stress. It must now be answered how LSP could have reduced GND density gradient and thus back stress in the rolled specimens.

Reduction in GND density gradient due to LSP beneath a marginal GND density increase near the treated surface may be attributed to dislocation annihilation and recrystallization caused by compressive shock. In annealed materials, the dislocation motion

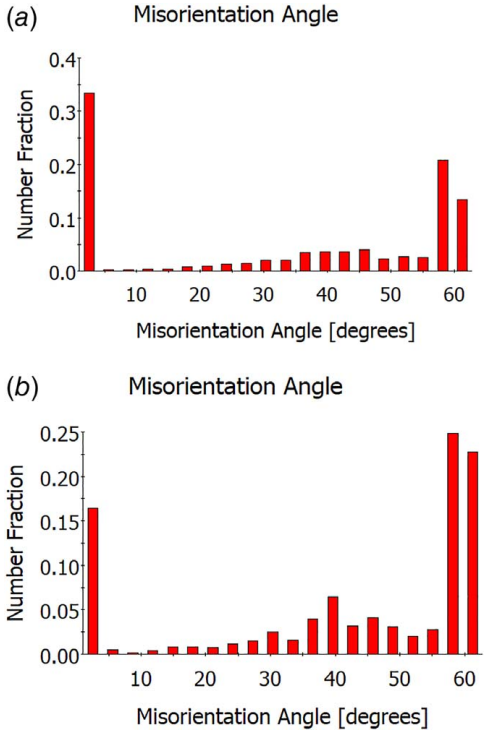

Fig. 11 Misorientation-angle histogram of the grains on the unstrained top surface of (*a*) the as-received sample and (*b*) the LSPed sample. Misorientation above 15 deg is considered a HAGB. The LSPed sample shows a distinctly higher representation of HAGBs which indicates recrystallization by dislocation annihilation.

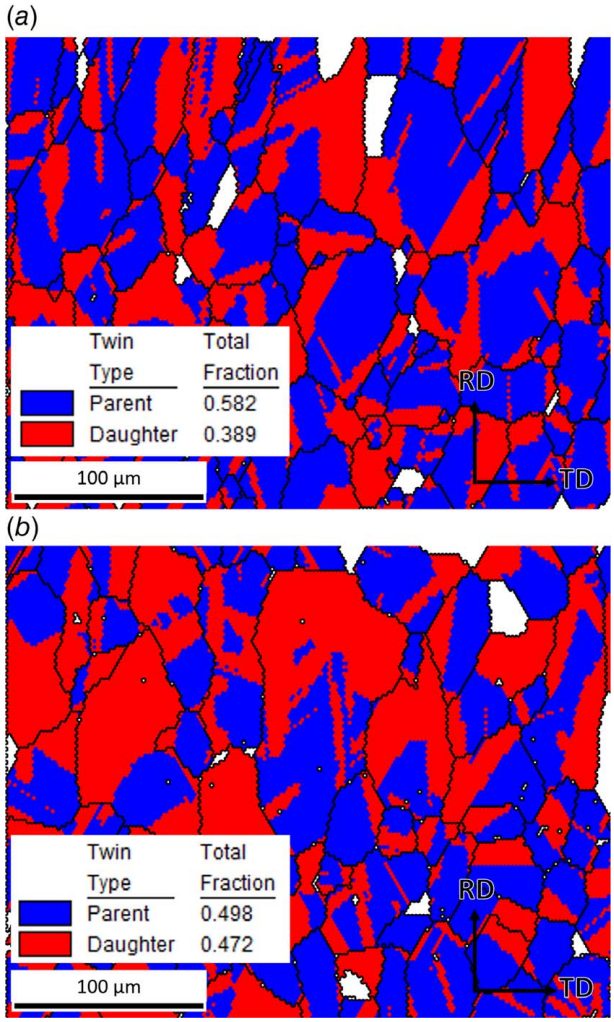

Fig. 12 Representative parent–daughter images of the unstrained top surface of (*a*) the as-received sample and (*b*) the LSPed sample. The white regions are nontwinned grains and the total fractions of parent and daughter twins are out of total twinned area. Recrystallization twinning is identified as a 60 deg rotation about the <111> axis in austenite. LSPed scans show a greater representation of daughter grains than in the as-received samples indicating recrystallization due to dislocation shock wave expansion.

due to LSP causes grain refinement as dislocation wave fronts expand from the cite of impact, forming cells, and subsequently subgrain and grain boundaries [20]. This expansion of dislocations typically induces a marked increase in dislocations near the surface of the material [35]. In rolled steel with dislocation structures that contribute to characteristic anisotropic back stress, the expanding cells created by LSP may break apart sessile tangles deeper under the surface and show a reduction in GND density, especially in newly formed grains. Recrystallization is known to reduce GNDs and high-power LSP induces grain refinement in 304 steel [33,45,46]. It is therefore reasonable to construe that recrystallization due to LSP is a driving force in the observed dislocation reduction. Dislocation annihilation may also result from a similar mechanism to GND density reduction observed in load reversal. Dislocation cells made by tensile prestain at low and high temperatures can be unstable upon compression, such that immediately after small amounts of compressive plastic strain the material also shows a reduction in GNDs [47,48]. Dislocation annihilation has been observed in unloading and load reversal during metal-forming spring-back as well [49,50]. Compressive stress caused by LSP acts similarly to this load reversal, neutralizing obstacles prevalent in the material's microstructure.

Subsurface Recrystallization. Recrystallization as a source of dislocation reduction can be evinced by multiple forms of EBSD analysis. The misorientation-angle histograms are given in Fig. 11. These histograms also make evident an increase in the high-angle grain boundaries above 25 deg. Such an increase in high-angle boundaries indicates recrystallization [33]. High-angle grain boundaries (HAGBs) have been characterized as misorientation exceeding 15 deg which also matches the IPF imaging. HAGBs may result from recrystallization under plastic strain and correlate with recrystallization in LSPed 304L [33,51]. While this increased representation of HAGBs in the LSPed sample is not sustained through tensile testing, the effects of the reduction to back stress are lasting.

Recrystallization twinning due to LSP can be directly observed through characterization within the EDAX TSL OIM software. The primary recrystallization twinning mode of FCC is identified as a 60 deg rotation about the <111> axis [52]. This identification can be used to show parent–daughter recrystallization in the as-received and LSPed scans. Figure 12 presents two representative scans. The original grain boundaries are given in black. The LSPed material has a larger area fraction occupied by twinning daughter grains which, when compared with the IPF image of the same scans in Fig. 9, are shown to be many of the more equiaxed grains. This form of twinning occurs during primary recrystallization as a low fault-energy mis-stack of newly formed lattice planes [45]. Dislocation cells grow and form boundaries, creating new grains with low dislocation density and as the lattice planes stack, recrystallization twins occur. Recrystallization likely also generates a more equiaxed grain morphology which further may cause a decrease in bulk back stress.

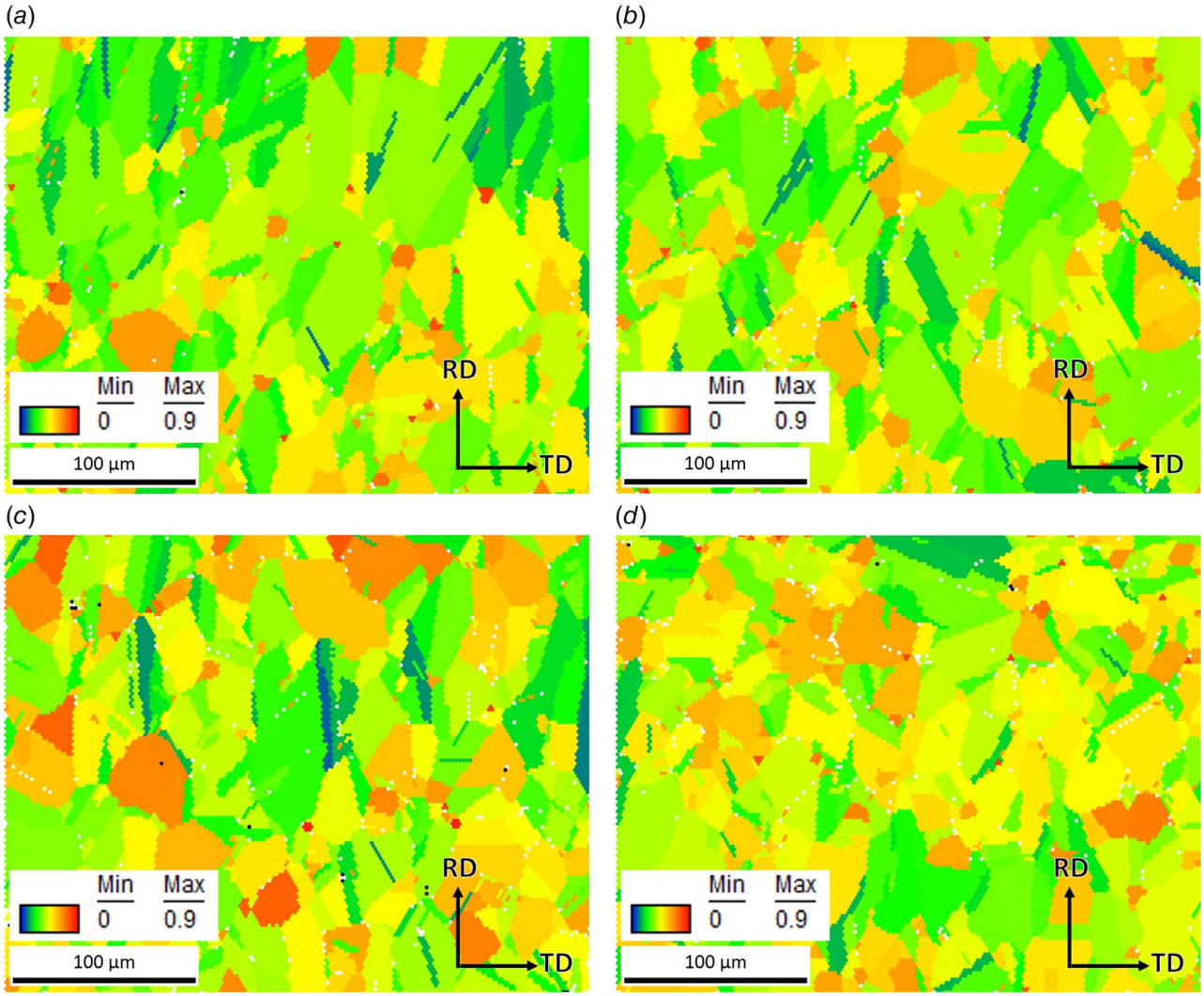

Fig. 13 Aspect ratio images of the top surface in the as-received samples in (*a*) unstrained and (*b*) 4% strained conditions and LSPed samples in (*c*) unstrained and (*d*) 4% strained conditions. An increase in the area occupied by equiaxed grains in the LSPed samples directly results in a decrease of bulk-averaged back stress as derived analytically using the Eshelby inclusion solution.

Aspect Ratio. Grain morphology is known to be a fundamental factor in the inter and intra-granular stress state of a polycrystalline material. As viewed in Fig. 13, the microstructure is significantly more equiaxed after LSP. A single-tailed Student *t*-test of the aspect ratios for the grains of the unstrained samples reveals a statistically significant difference between LSPed and as-received conditions at a 95% confidence interval (CI). The mean aspect ratio of the LSPed grains is 0.454 with a sample size of 525 grains and a standard deviation of 0.141. The mean aspect ratio of the as-received sample is 0.429 with 586 grains and a standard deviation of 0.144. Furthermore, as seen in Figs. 13(*a*) and 13(*c*), the equiaxed grains in the LSPed sample dominate a larger proportion of the area fraction. The strained LSPed sample has a higher average aspect ratio than the strained as-received sample with a mean of 0.422 as compared with 0.415. The grain population is 412 in the LSPed strained sample and 426 in the as-received strained sample; the standard deviations are 0.147 and 0.155 respectively. At a 95% confidence this difference does not prove statistically significant. After uniaxial tension, plastic strain along the pulling direction dominates the samples grain structure.

The increase in the aspect ratio in the LSPed material independently reduces long-range back stress. This is because higher aspect ratio inherently increases the back stress within a grain all else equal. Back stress along an axis of a grain is equal to the shear stress resisting twinning. The Eshelby inclusion solution for shear stress within a penny-shaped grain in an elastic continuum is known [53]. From this derivation, back stress can be calculated as the following:

$$\alpha = \frac{\nu - 2}{4(1-\nu)} \pi \frac{a_2}{a_1} \, s \tag{8}$$

where ν = Poisson's ratio, a_2 = the transverse grain diameter, a_1 = the grain diameter along the axis of tension, and s = the twinning shear. The elongated grains in the as-received material are seen to have their largest diameter along the tension direction. Thus, an increase in the aspect ratio decreases the a_2/a_1 component of the back stress. The tendency of the recrystallized grains in the LSPed material to be more equiaxed therefore inherently reduces back stress.

Conclusion

Laser shock peening reduces back stress by primarily creating compressive plastic strain in the surface of the material which is a well-known result in literature. This effect causes dislocations to pile up at obstacles to compressive yield, causing the yield surface to shift or elongate in the compressive direction. Upon

tensile loading, the dislocations run away from these compressive obstacles and cause tensile yield at a lower stress than compressive yield. Isotropic hardening combined with kinematic hardening may occur, however the yield asymmetry of a sample with tensile back stress is reduced. An improved aspect ratio due to grain shape changes also contributes to reducing back stress. More broadly, LSP mitigates yield asymmetry in rolled stainless steel by augmenting the surface characteristics of the part through three mechanisms: (1) compressive residual stress, (2) compressive back stress, and (3) recrystallization. LSP-induced compressive residual stress has been established by others as the primary mode of fatigue life improvement. This compressive stress also resists tensile loading, causing the yield surface of the metal to be displaced in the compressive direction. LSP also causes surface-level compressive back stress as shown by experiments and FEA modeling established nonlinear hardening theory. The compressive back stress neutralizes existing tensile back stress when bulk averaged and reduces the back stress developed during tensile load. Beneath the surface hardened layer of the LSP-treated parts, the GND density is less before and after plastic straining, correlating with the measured back stress reduction. Grain morphology analysis shows evidence of recrystallization which both alleviates residual morphological anisotropy due to rolling and also likely contributes to the reduction of dislocations. This paper demonstrates LSP may be applied to rolled stainless steel to overcome the problems presented by yield asymmetry in addition to the already well-known effect of fatigue life improvement.

Acknowledgment

Financial support from the NSF under grant #1761344 and the NSF graduate research fellowship is much appreciated. We would also like to acknowledge the Materials Research Science and Engineering Center funded by NSF at Columbia University for the use of its shared facilities.

Conflict of Interest

There are no conflicts of interest.

Data Availability Statement

The datasets generated and supporting the findings of this article are obtainable from the corresponding author upon reasonable request.

References

[1] Battelle Memorial Institute, 2020, *Metallic Materials Properties Development and Standardization (MMPDS-15)*, Battelle Memorial Institute, Columbus, OH.
[2] Shintani, T., and Murata, Y., 2011, "Evaluation of the Dislocation Density and Dislocation Character in Cold Rolled Type 304 Steel Determined by Profile Analysis of X-Ray Diffraction," Acta Mater., **59**(11), pp. 4314–4322.
[3] Charpentier, P. L., 2015, "Post-Forming Monotonic and Cyclic Behavior in HSLA Steel Sheet After Large Deformations in-Plane Compression," Int. J. Fatigue, **79**, pp. 54–64.
[4] Charpentier, P. L., 2019, "Post-Forming Room Temperature Brittle Fracture in a High-Strength Low Alloy Steel Sheet After Various Forming Modes," J. Mater. Eng. Perform., **28**, pp. 7119–7140.
[5] Mehrabi, H., Ya-ng, R. C., and Wang, B., 2020, "Effects of Tension-Compression Asymmetry on Bending of Steels," Appl. Sci., **10**(9), p. 3339.
[6] Barros, P. D., Alves, J. L., Oliveira, M. C., and Menezes, L. F., 2018, "Study on the Effect of Tension-Compression Asymmetry on the Cylindrical Cup Forming of an AA2090-T3 Alloy," Int. J. Solids Struct, **151**, pp. 135–144.
[7] Garud, C., Benedyk, J., Mostovoy, S., and Nash, P., 2005, "Evaluating the Bauschinger Effect in Heavily Cold Worked 301 Austenitic Stainless Steel Used in Multi-Layer Head Gaskets," SAE 2005 World Congress & Exhibition, Detroit.
[8] Chen, J., Yao, W., and Gao, D., 2020, "Fatigue Life Evaluation of Tension-Compression Asymmetric Material Using Local Stress-Strain Method," FFEMS, **43**(9), pp. 1994–2005.
[9] Meininger, J. M., Dickerson, S. L., and Gibeling, J. C., 1996, "Observations of Tension/Compression Asymmetry in the Cyclic Deformation of Aluminum Alloy 7075," FFEMS, **19**(1), pp. 85–97.
[10] Li, X., Cheng, C., Le, Q., Zhou, X., Liao, Q., Chen, X., and Jia, Y., 2019, "Ex-Situ EBSD Analysis of Yield Asymmetry, Texture and Twinning Development in Mg-5Li-3Al-2Zn Alloy During Tensile and Compressive Deformation," J. Alloys Compd., **805**, pp. 947–956.
[11] Lin, P., Hao, Y., Zhang, B., Zhang, S., Chi, C., and Shen, J., 2017, "Tension-Compression Asymmetry in Yielding and Strain Hardening Behavior of CP-Ti at Room Temperature," Mater. Sci. Eng. A, **707**, pp. 172–180.
[12] Gall, K., and Sehitoglu, H., 1999, "The Role of Texture in Tension-Compression Asymmetry in Polycrystalline NiTi," Int. J. Plast, **15**(1), pp. 69–92.
[13] Davis, A. E., Robson, J. D., and Turski, M., 2019, "Reducing Yield Asymmetry and Anisotropy in Wrought Magnesium Alloys—A Comparative Study," Mater. Sci. Eng. A, **744**, pp. 525–537.
[14] Wang, J., Li, X., Jin, P., Li, S., Ma, G., and Zhao, L., 2019, "Reducing the Tension-Compression Yield Asymmetry in an Extruded ZK60 Alloy by Ultrafine Grains," Mater. Res. Express, **5**(11), p. 116518.
[15] Tong, L. B., Zheng, M. Y., Kamado, S., Zhang, D. P., Meng, J., Cheng, L. R., and Zhang, H. J., 2015, "Reducing the Tension-Compression Yield Asymmetry of Extruded Mg-Zn-Ca Alloy via Equal Channel Angular Pressing," J. Magnes. Alloy, **3**(4), pp. 302–308.
[16] Wei, J., You, J., Zhang, D., Jiang, S., Chen, Z., and Liu, C., 2020, "Reducing Yield Asymmetry in Wrought Mg-9Al Alloy by Randomized Texture Achieved via Multi-Directional Forging," Mater. Sci. Eng. A, **796**, p. 140003.
[17] Chen, H. B., Liu, T. M., Zhang, Y., Zhai, Y. B., and He, J. J., 2016, "Reducing Tension-Compression Yield Asymmetry by Free End Torsion in Extruded Mg Alloy," Mater. Sci. Tech, **32**(2), pp. 111–118.
[18] Ellermann, A., and Scholtes, B., 2011, "The Bauschinger Effect in Different Heat Treatment Conditions of 42CrMo4," Int. J. Solids Struct, **3**(1), pp. 1–13.
[19] Clauer, A. H., 1997, "Laser Shock Peening for Fatigue Resistance," Conference on Surface Performance of Titanium, Cincinnati, OH, January.
[20] Wang, C., Wang, L., Wang, C.-L., Li, K., and Wang, X.-G., 2019, "Dislocation Density-Based Study of Grain Refinement Induced by Laser Shock Peening," Opt. Laser Technol, **121**, p. 105827.
[21] Pan, X., Wang, X., Tian, Z., He, W., Shi, X., Chen, P., and Zhou, L., 2021, "Effect of Dynamic Recrystallization on Texture Orientation and Grain Refinement of Ti6Al4V Titanium Alloy Subjected to Laser Shock Peening," J. Alloy Compd, **850**, p. 156672.
[22] Peyre, P., and Fabbro, R., 1995, "Laser Shock Processing: A Review of the Physics and Applications," Opt. Quantum Electron., **27**, pp. 1213–1229.
[23] Long, J., Pan, Q., Tao, N., and Lu, L., 2018, "Residual Stress Induced Tension-Compression Asymmetry of Gradient," Mater. Res. Lett, **6**(8), pp. 456–461.
[24] Hill, R., 1950, *The Mathematical Theory of Plasticity*, Clarendon Press, Oxford, UK, Chap. 2.
[25] Cottrell, A. H., 1953, *Dislocations and Plastic Flow in Crystals*, Oxford University Press, London, UK, Chap. 9.
[26] Sowerby, R., Uko, D. K., and Tomita, Y., 1979, "A Review of Certain Aspects of the Bauschinger Effect in Metals," Mat. Sci. Eng., **41**(1), pp. 43–58.
[27] Yang, M., Pan, Y., Yuan, F., Zhu, Y., and Wu, X., 2016, "Back Stress Strengthening and Strain Hardening in Gradient Structure," Mat. Res. Lett, **4**(3), pp. 145–151.
[28] Ashby, M. F., 1970, "The Deformation of Plastically Non-Homogeneous Materials," Philos. Mag. Lett, **21**(170), pp. 399–424.
[29] Field, D. P., Trivedi, P. B., Wright, S. I., and Kumar, M., 2005, "Analysis of Local Orientation Gradients in Deformed Single Crystals," Ultramicroscopy, **103**(1), pp. 33–39.
[30] El-Dasher, B. S., Adams, B. L., and Rollett, A. D., 2003, "Viewpoint: Experimental Recovery of Geometrically Necessary Dislocation Density in Polycrystals," Scr. Mater, **48**(2), pp. 141–145.
[31] Hansen, L. T., Fullwood, D. T., Homer, E. R., Wagoner, R. H., Lim, H., Carroll, J. D., Zhou, G., and Bong, H. J., 2019, "An Investigation of Geometrically Necessary Dislocations and Back Stress in Large Grained Tantalum via EBSD and CPFE," Mater. Sci. Eng. A, **777**, p. 138704.
[32] Sikhamov, R., Fomin, F., Klusemann, B., and Kashaev, N., 2020, "The Influence of Laser Shock Peening on Fatigue Properties of AA2024-T3 Alloy With a Fastener Hole," Metals, **10**(4), 495.
[33] Lu, J. Z., Deng, W. W., Luo, K. Y., Wu, L. J., and Lu, H. F., 2017, "Surface EBSD Analysis and Strengthening Mechanism of AISI 304 Stainless Steel Subjected to Massive LSP Treatment With Different Pulse Energies," Mater. Charact., **125**, pp. 99–107.
[34] Clauer, A. H., and Holbrook, J. H., 1981, *Shock Waves and High-Strain-Rate Phenomena in Metals*, M. Meyers, ed., Plenum Publishing Corporation, New York, Plenum, pp. 675–703.
[35] Brandal, G., and Yao, Y. L., 2017, "Material Influence on Mitigation of Stress Corrosion Cracking via Laser Shock Peening," ASME J. Manuf. Sci. Eng., **139**(1), p. 011002.
[36] Shadangi, Y., Chattopadhyay, K., Rai, S. B., and Singh, V., 2015, "Effect of Laser Shock Peening on Microstructure, Mechanical Properties and Corrosion Behavior of Interstitial Free Steel," Surf. Coat. Technol., **280**, pp. 216–224.
[37] Kalentics, N., Huang, K., Ortega Varela de Seijas, M., Burn, A., Romano, V., and Loge, R. E., 2019, "Laser Shock Peening: a Promising Tool for Tailoring Metallic Microstructures in Selective Laser Melting," J. Mater. Process. Technol., **266**, pp. 612–618.

[38] Lin, C. C., and Hu, C. C., 2008, "Electropolishing of 304 Stainless Steel: Surface Roughness Control Using Experimental Design Strategies and Summarized Electropolishing Model," Electrochim. Acta, **53**(8), pp. 3356–3363.
[39] Zhang, W., and Yao, Y. L., 2002, "Micro Scale Laser Shock Processing of Metallic Components," ASME J. Manuf. Sci. Eng., **124**(2), pp. 369–378.
[40] Fabbro, R., Fournier, J., Ballard, P., Devaux, D., and Virmont, J., 1990, "Physical Study of Laser-Produced Plasma in Confined Geometry," J. Appl. Phys, **68**(2), pp. 775–784.
[41] Hibbit, D., Karlsson, B., and Sorenson, P., 2019, *Abaqus 6.19: Theory Manual*, Dassault Systemes, Providence, RI.
[42] Bjørn, H., 2019, "Bauschinger Effect Modelled by Yield Surface Distortions," Int. J. Plast, **123**, pp. 86–100.
[43] Jin, H., Sanborn, B., Lu, W. Y., and Song, B., 2021, "Mechanical Characterization of 304L-VAR Stainless Steel in Tension With Coverage of Low, Intermediate and High Strain Rates," Mech. Mater, **152**, p. 103654.
[44] Fan, Y., Wang, Y., Vukelic, S., and Yao, Y. L., 2005, "Wave-Solid Interactions in Laser-Shock-Induced Deformation Processes," J. Appl. Phys, **98**(10), p. 104904.
[45] Cahn, R. W., 1996, *Physical Metallurgy (Fourth, Revised and Enhanced Edition), Department of Materials Science and Metallurgy*, R. W. Cahn, and P. Haasen, eds., University of Cambridge, Cambridge, UK, pp. 2399–2500.
[46] Salehi, M. S., Anjabin, N., and Kim, H. S., 2019, "Study of Geometrically Necessary Dislocations of a Partially Recrystallized Aluminum Alloy Using 2D EBSD," Microsc. Microanal, **25**(3), pp. 656–663.
[47] Hasegawa, T., Yakou, T., and Karashima, S., 1975, "Deformation Behaviour and Dislocation Structures Upon Stress Reversal in Polycrystalline Aluminum," Mater. Sci. Eng. A, **20**, pp. 267–276.
[48] Hasegawa, T., and Yakou, T., 1986, "Forward and Reverse Rearrangements of Dislocations in Tangled Walls," Mater. Sci. Eng. A, **81**, pp. 189–199.
[49] Ghosh, A. K., 1980, "A Physically-Based Constitutive Model for Metal Deformation," Acta Metall. Mater., **28**(11), pp. 1443–1465.
[50] Cleveland, R. M., and Ghosh, A. K., "Inelastic Effects on Springback in Metals," Int. J. Plast, **18**(5–6), pp. 769–785.
[51] Valeyev, I., Kaibyshev, R., Sitdikov, O., and Sokolov, B., 1990, "The Formation of High Angle Grain Boundaries During the Plastic Deformation of Magnesium and Magnesium Alloys," J. Phys. Colloq, **51**(C1), pp. C1-673–C1-677.
[52] EDAX, 2018, *OIM Analysis*, Amtek Inc., Materials Analysis Division, Mahwah, NJ.
[53] Mura, T., 1925, *Micromechanics of Defects in Solids*, Kluwer Academic Publishers, Dordrecht.